Lithuanian Journal of Physics
Vol. **63**, No. 4, pp. 210–217 (2023)
ISSN 1648-8504 eISSN 2424-3647
DOI: https://doi.org/10.3952/physics.2023.63.4.3

# ON NONPARAXIAL SINGLE-PIXEL IMAGING OF SEMITRANSPARENT OBJECTS USING FLAT DIFFRACTIVE OPTICS

**P. Kizevičius [a], S. Orlov [a], K. Mundrys [a], V. Jukna [a], L. Minkevičius [b], and G. Valušis [b]**

[a] *Department of Fundamental Research, Center for Physical Sciences and Technology, Saulėtekio 3, 10257 Vilnius, Lithuania*
[b] *Department of Optoelectronics, Center for Physical Sciences and Technology, Saulėtekio 3, 10257 Vilnius, Lithuania*
Email: sergejus.orlovas@ftmc.lt

Received 28 September 2023; accepted 2 October 2023

High numerical apertures can result in distortions appearing in a single-shot image, rendering the acquisition of usable images challenging, if not outright impossible. However, in the realm of single-pixel imaging, various strategies can be employed to effectively inspect objects with an excellent resolution, contrast and brightness. Recent advancements in flat photonic components have facilitated the development of compact nonparaxial imaging systems, which show great promise, particularly in the THz range of wavelengths. These innovations hold the potential to advance fields such as communication, material inspection and spectroscopy. In this study, we delve into the imaging of semi-transparent objects with varying levels of detail. Furthermore, we introduce a nonparaxial design for a flat hyperbolical lens and evaluate its performance in these imaging scenarios, comparing it to structured illumination techniques involving Airy, Bessel, and common thin lens configurations. We present findings regarding potential improvements in imaging attributable to the nonparaxial hyperbolical lens.

**Keywords:** nonparaxial imaging, single-pixel imaging, contrast, resolution

## 1. Introduction

Image retrieval, originating with the invention of cameras, now relies on digital sensors with millions of pixels. However, single-pixel detectors, which measure scene overlap with masks and combine the data, offer an alternative approach validated both theoretically and experimentally, even extending to 3D reconstruction [1–6]. This concept has historical roots dating back to 19th century, with the mathematical theory of raster scan systems developed in 1934 [7–9]. Ghost imaging, a related computational technique, leverages computational algorithms for data processing, offering advantages in detection efficiency and noise reduction [3]. Single-pixel and ghost imaging are optically similar, using spatial light modulators (SLMs) for structured illumination [4–6]. Structured electromagnetic fields, exemplified by nondiffracting beams with vortical and polarization properties, find applications in communication, metrology and light–matter interactions [10–12]. These beams enhance imaging, even in the THz range, where laser-fabricated flat optics and structured illumination show promise [13, 14].

Our work builds on recent advances in single-pixel raster scan imaging, with the aim of improving resolution assessment by employing a sample with fine-tuned line widths [15]. Through numerical experimentation in nonparaxial imaging, we have discussed contrast and resolution, revealing a noteworthy discovery: in nonparaxial single-pixel imaging, the best resolution does not depend on image brightness [15]. This challenges the established physical metrics, prompting the use of image quality assessment metrics from computational imaging. Surprisingly, the high resolution can coexist with the low image brightness [14]. These findings raise critical questions, demanding further numerical and experimental exploration [14].

In this report, we introduce two semi-transparent samples with varying levels of transmittivity

(ranging from 0 to 1) and details with dimensions ranging from comparable to the wavelength and smaller than the wavelength. Both samples are investigated under nonparaxial single-pixel illumination conditions, which were discussed in our recent work [14]. Additionally, we introduce a flat element with the nonparaxial phase mask of a hyperbolical lens and benchmark it extensively against Bessel, Airy and common zone plates. Whereas the Bessel and Airy structured illumination performs better than a zone plate, the nonparaxial hyperbolical lens shows promising enhancements over all other elements.

## 2. Theoretical background

Our numerical experimentation mimics experiments performed using a typical THz wavelength $\lambda$ = 0.5 mm, or a frequency of 0.6 THz. The flat optical elements used in these experiments have apertures of 20 mm diameter. Our main aim is to perform a visual inspection of a semi-transparent sample under conditions reported in this work [14]. For this purpose, we provide focusing and imaging abilities using a flat element with the phase $\Psi(\mathbf{r})$ of the transmission function $T(\mathbf{r}) = \exp[\mathrm{i}\Psi(\mathbf{r})]$. Here, $\Psi(x, y)$ is a continuous phase profile of the designed element. Firstly, we design a thin lens with the phase of the transmission function

$$\Psi_{\mathrm{TL}}(\mathbf{r}) = \frac{k}{2f}(x^2 + y^2), \tag{1}$$

where $f$ = 1 cm is the focal length and $k = 2\pi/\lambda$.

Next, the linear phase function represents the axicon element

$$\Psi_{\mathrm{B}}(\mathbf{r}) = \frac{2\pi \sin\beta}{\lambda}\sqrt{x^2 + y^2}, \tag{2}$$

where $\beta$ = 0.4 rad.

Third, a cubic phase profile is used to generate a structured Airy illumination

$$\Psi_{\mathrm{AI}}(\mathbf{r}) = a(x^3 - y^3). \tag{3}$$

This design represents a phase mask of diameter 20 mm, which together with a zone plate ($f$ = 1 cm) is dedicated to generating an Airy beam in a range of up to 10 mm.

Lastly, we introduce a nonparaxial hyperbolical lens [16] encoded as

$$\Psi_{\mathrm{HL}}(\mathbf{r}) = k\sqrt{f^2 + x^2 + y^2}, \tag{4}$$

where $f$ = 1 cm is the focal length.

We introduce the nonparaxial Rayleigh–Sommerfeld diffraction integral [17]

$$U_1(\mathbf{r}_1) = \frac{1}{\mathrm{i}\lambda}\int_{S_\mathrm{A}} U_{\mathrm{inc}}(\mathbf{r}_0)T(\mathbf{r}_0) \times \frac{\exp[\mathrm{i}k\,|\,\mathbf{r}_{01}\,|]}{|\,\mathbf{r}_{01}\,|}\cos(\mathbf{r}_{01}, \mathbf{n})\mathrm{d}S, \tag{5}$$

where $U_1(\mathbf{r}_1)$ is the field in the observation plane, $U_{\mathrm{inc}}(\mathbf{r}_0)$ is the incident field in the diffraction plane, and $T(\mathbf{r}_0)$ is the transmittance of the object. The coordinates of the diffraction plane are $\mathbf{r}_0 = (x_0, y_0, z = 0)$ and the coordinates of the observation plane are $\mathbf{r}_1 = (x_1, y_1, z = z_1)$, the vector $\mathbf{r}_{01}$ is the distance between two points in these planes, and $\mathbf{n}$ is normal to the surface of the object. Integration is performed on the surface of the element $S_\mathrm{A}$. On the basis of this consideration, we have employed a propagator using spherical point sources to numerically model the propagation of the electromagnetic field within the system.

The numerical experiment is performed as follows. First, Eq. (5) is applied to propagate the electromagnetic field of the incident radiation from the first lens to the sample (see Fig. 1). Next, the resulting field $U_1(\mathbf{r}_1)$ is multiplied by the object transmission function $T_{\mathrm{obj}}(\mathbf{r}_1)$ and the field is propagated to the second lens (see Fig. 1),

$$U_2(\mathbf{r}_2) = \frac{1}{\mathrm{i}\lambda}\int_{S_\mathrm{A}} U_1(\mathbf{r}_1)T_{\mathrm{obj}}(\mathbf{r}_1) \times \frac{\exp[\mathrm{i}k\,|\,\mathbf{r}_{12}\,|]}{|\,\mathbf{r}_{12}\,|}\cos(\mathbf{r}_{12}, \mathbf{n})\mathrm{d}S, \tag{6}$$

where the coordinates $\mathbf{r}_2 = (x_2, y_2, z = z_2)$ are the coordinates of the plane of the second lens. The vector $\mathbf{r}_{12}$ is the distance between two points in these planes, and $\mathbf{n}$ is normal to the surface of the sample.

Lastly, the electromagnetic field $U_2(\mathbf{r}_2)$ multiplies with the transmission function of the second lens and propagates to the single-pixel detector, located at $\mathbf{r}_3 = (x_3 = 0, y_3 = 0, z = z_3)$:

$$U_3(\mathbf{r}_3) = \frac{1}{\mathrm{i}\lambda}\int_{S_\mathrm{A}} U_2(\mathbf{r}_2)T(\mathbf{r}_2) \times \frac{\exp[\mathrm{i}k\,|\,\mathbf{r}_{23}\,|]}{|\,\mathbf{r}_{23}\,|}\cos(\mathbf{r}_{23}, \mathbf{n})\mathrm{d}S. \tag{7}$$

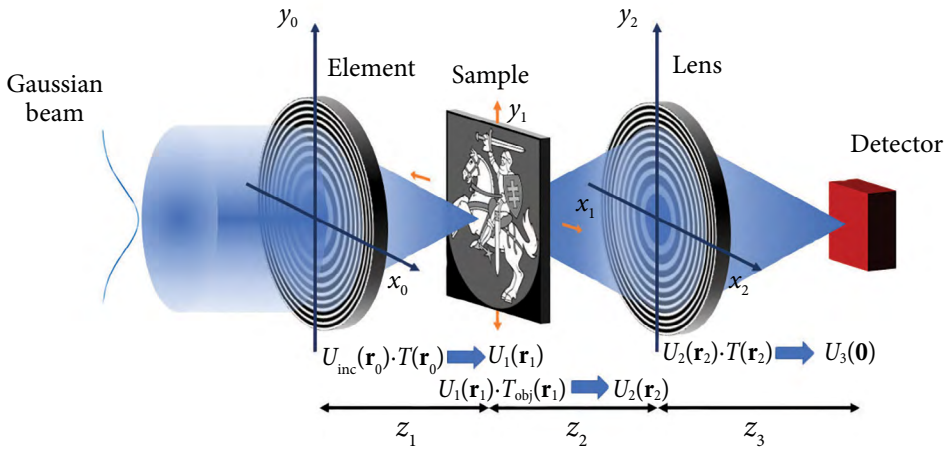


Fig. 1. A schematic representation of the setup for numerical experimentation. The spherical wave propagator is successively applied three times: 1) to calculate the propagation from the plane $(x_0, y_0)$ to the plane of the object $(x_1, y_1)$, 2) to calculate the propagation from the plane $(x_1, y_1)$ to the plane of the object $(x_2, y_2)$ and 3) to calculate the propagation from the plane $(x_2, y_2)$ to the single-pixel detector $(x_3, y_3) = (0, 0)$. The detector is a single-pixel camera. The sample is scanned by raster in the $x_1$ and $y_1$ directions (orange arrows).

The operation is consecutively performed for different positions of the sample, which is raster-scanned in the $x_2$ and $y_2$ directions. This is the theoretical basis for our further numerical experimentation.

We note that the numerical simulations involving the Airy phase mask require an additional step, because the element in Fig. 1 is replaced by the cubic Airy mask (3) and a thin lens (1) separated by a distance of 1 cm.

## 3. Dissection of numerical experiments

We select an imaging sample motivated by our recent research (see Ref. [14]). In this research, we have benchmarked the resolution of various structured illumination setups using a sample containing 12 groups of four lines with different line widths of black and white strips. Nevertheless, the question is still open as to how these various imaging systems will perform when a sample is an actual image with varying levels of transparency and fine details. In order to answer this question, we have prepared two samples containing different modulation levels of transmittance with varying degrees of spatial details (see Fig. 2). We recall that the wavelength of the electromagnatic radiation is $\lambda = 0.5$ mm; thus, the approximate size of the imaging sample is approximately 100 wavelengths.

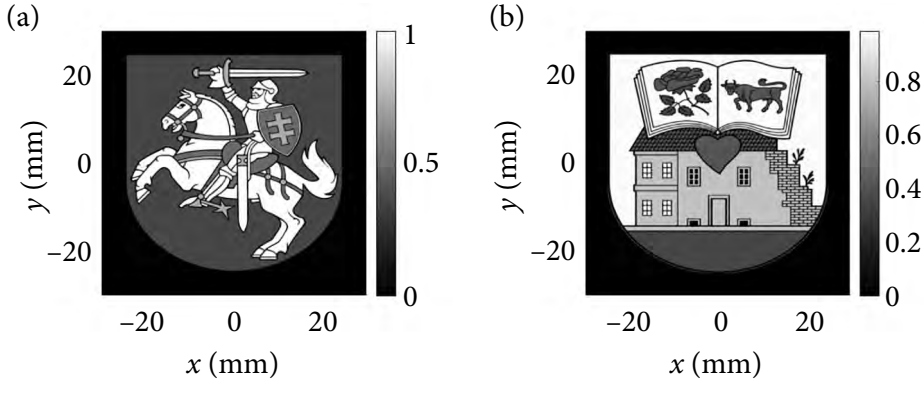


Fig. 2. Two imaging samples (with sizes of 50 mm) used in further numerical experimentations: the coat of arms of Lithuania (a) and the coat of arms of Ukmergė (b). Colour bars represent the transmittivity of the imaging sample.

To demonstrate the problems that arise from conventional nonparaxial imaging, we performed a numerical simulation of the sample imaging using a paraxial thin lens (see Eq. (1)) and a nonparaxial lens (see Eq. (4)) under conditions of THz illumination with a wavelength of $\lambda = 0.5$ mm and an optical wavelength of $\lambda = 0.5$ $\mu$m. We used lenses with focal lengths of 1 cm and placed the object 2 cm away from the lens. The image was recorded at a distance of 2 cm from the lens so as not to have a magnification of the image. The results are depicted in Fig. 3, please note the reversal of the axis as the image is inverted in the image plane.

First, we note that under optical illumination, due to the small wavelength, both samples are imaged properly (see Fig. 3 (a, d)). Images of both objects are 50 mm in size, as expected. As we move to the THz wavelengths, the single-shot images become hugely distorted (Fig. 3(b, c, e, f)). The thin lens is able to image only very small regions in the centre of the samples, but it fails overall. Even the general form of the sample is completely distorted and unrecognizable. This is an expected behaviour due to two factors: first, the thin lens is just a paraxial approximation, which in an expected manner fails the test. Second, because of the rather large wavelength of the THz radiation, the single-shot imaging process becomes a nonparaxial process, where rays travelling from different parts of the sample at different angles will not arrive at the same time to the imaging plane.

Single-shot imaging using the nonparaxial hyperbolical lens performs slightly better, as at least the outer form of both coats of arms is recognizable (see Fig. 3(c, f)). We even manage to recognize some smaller inner structures; however, the shortcomings of the single-shot imaging become obvious.

With this in mind, we proceed now to numerical simulations in the following setup (see Fig. 1). This is a general setup, largely mimicking the experimental setup from Ref. [14]. The sample is placed at the distance $z_1$ from element 1, which is an element with the phase transmission function, described using Eqs. (1–4). We did a raster scan of

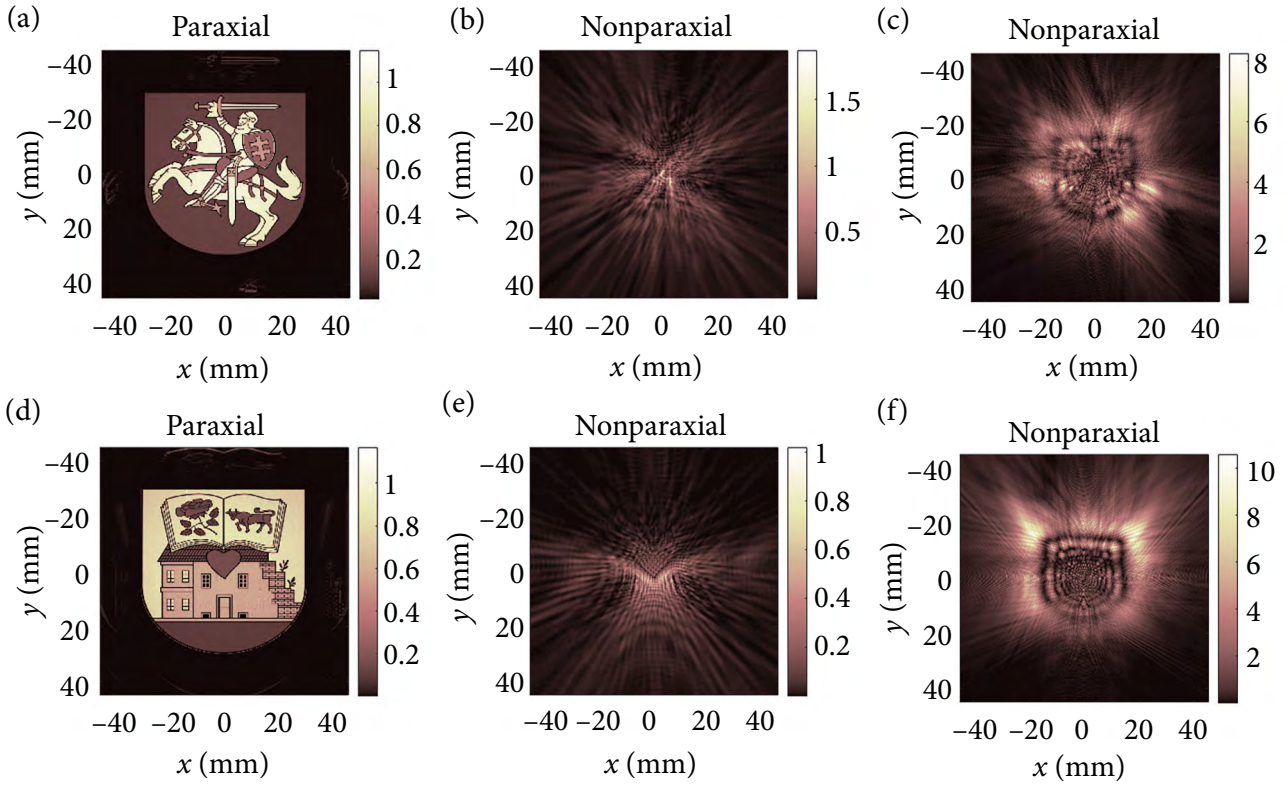


Fig. 3. Optical (a, d) and THz (b, c, e, f) single shot imaging of semitransparent samples: the coat of arms of Lithuania (a–c) and the coat of arms of Ukmergė (d–f). Colour bars represent the recorded intensity of the sample image. All samples are located 2 cm away from the thin lens (a, b, d, e) and the nonparaxial hyperbolical lens (c, f) with a focal distance of $f = 1$ cm. Images are recorded in the plane located 2 cm from the other side of lenses. Distances were chosen as not to have any magnification.

the two samples in the $x$ and $y$ directions and recorded the signal detected by the single pixel detector. A comparison of the images obtained using single-pixel imaging for one particular distance is given in Fig. 4. The conditions under which images are recorded are as follows.

In the case of thin lens illumination, the brightest focal spot formed at a distance of 8.5 mm from the lens; therefore, we have chosen this distance to place our sample ($z_1$ = 8.5 mm), see Fig. 1. Further, at the distance $z_2$ = 26 mm, the second collecting lens was placed. The single-pixel detector was located at the distance $z_3$ = 20 mm. The outcome of the raster scanning procedure is given in Fig. 4(a). We note immediately that in contrast to the single-shot imaging, the single-pixel THz imaging is capable of resolving not only the semitransparancy of the sample but also fine details. Of course, some very fine details are lost in the imagining process. Nevertheless, the sample is overall very well recognizable.

The second configuration did involve an axicon phase mask (see Eq. (2)). The brightest focal spot is formed at the distance $z_1$ = 12 mm; therefore we have placed the imaging object there (see Fig. 1). Furthermore, at the distance $z_2$ = 18 mm, the second collecting lens was placed. The single-pixel detector was located at the distance $z_3$ = 20 mm. The result of the raster scanning procedure is given in Fig. 4(b). Once again, in contrast to the single-shot imaging, we are able to record the sample with much better quality and even resolve the fine details. However, the picture at first sight seems to be of poorer quality than the one imaged with a single pixel thin lens, because of the lower image sharpness and blooming. However, the signal collected in the single-pixel camera seems to be stronger than in the previous simulation. This can be explained by the concept of modulation transfer function [18].

Within the theory of imaging, the perfect reproduction of the object, including sharp transitions at the edge of the pixel, is assumed, but this is never fully achieved in practice. Even a well-designed and manufactured lens cannot completely reproduce an object's resolution and contrast due to the nature

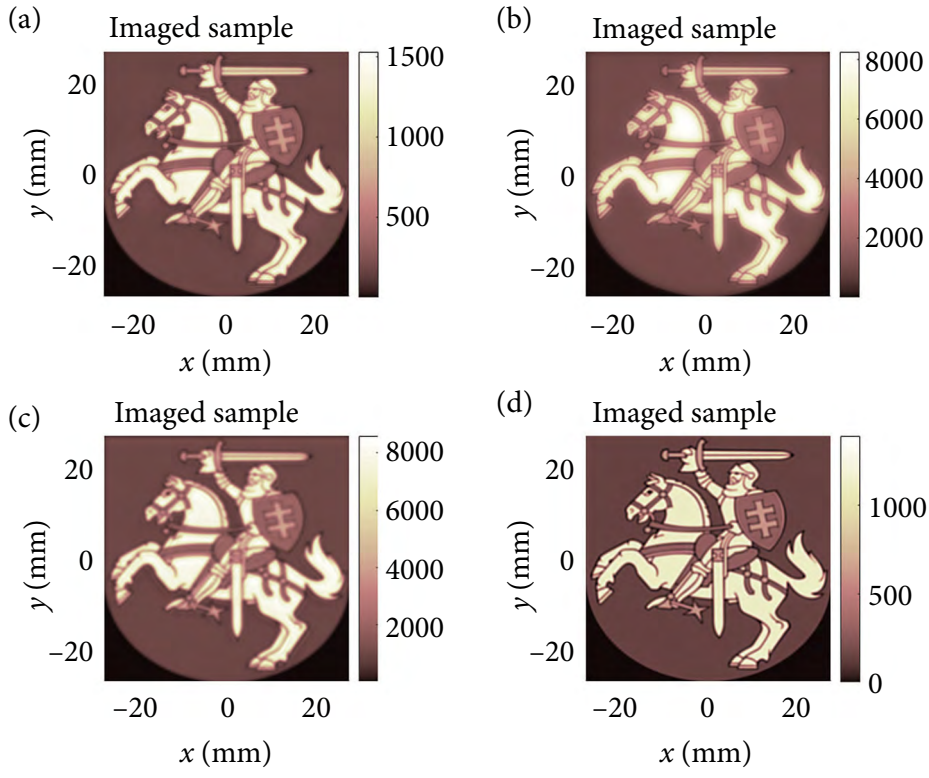


Fig. 4. Nonparaxial single-pixel THz imaging of the semitransparent sample coat of arms of Lithuania under different structured illuminations. Colour bars represent the recorded intensity of the sample image. The illumination is produced by the thin lens (a), the axicon (b), the Airy phase mask together with the lens (c) and the hyperbolical nonparaxial lens (d).

of light. The resolving power of the system depends on its ability to detect the space between objects. This ability is described by the modulation transfer function, which fundamentally indicates how modulations in the object are recorded by the imaging system in the recorded image.

The comparison of Fig. 4(a) and Fig. 4(b) reveals that the modulation transfer functions of thin lens and axicon behave differently in the sense that the lens images preserve a linear response to linear modulations in the object, but the modulation transfer of the axicon tends to result in a better resolution and finesse while distorting transmission levels of the object under inspection.

The third configuration uses the Airy phase mask (see Eq. (3)). The brightest focal spot is formed at the distance $z_1$ = 10 mm, therefore we have placed the image there (see Fig. 1). Further, at the distance $z_2$ = 26 mm, the second collecting lens was placed. The single-pixel detector was located at the distance $z_3$ = 20 mm. The result of the raster scanning procedure is given in Fig. 4(c). As we see, the structured Airy illumination results in the modulation transfer function, where the linearity in the response to the strength of the modulation is restored compared to the previous case (see Fig. 4(b)). Moreover, the fine details are better visible than in two previous cases.

Lastly, we investigate the performance of the nonparaxial hyperbolical lens (see Eq. (4)). The brightest focal spot is formed at the distance $z_1$ = 10 mm (see Fig. 1). The distances $z_2$ and $z_3$ are the same as before. The result of the raster scanning procedure is given in Fig. 4(d). To our surprise, the nonparaxial hyperbolical lens performs not only better than the thin lens but also better than the axicon and the Airy structured illumination, resulting in the brightest and sharpest recorded image. This finding is intriguing and requires further investigation.

Now we proceed to the investigation of the second sample, which has finer details with both large and small modulations in it. All distances $z_1$, $z_2$ and $z_3$ were kept as in the previous imaging run (see Fig. 1). The result of the raster scanning procedure is given in Fig. 5.

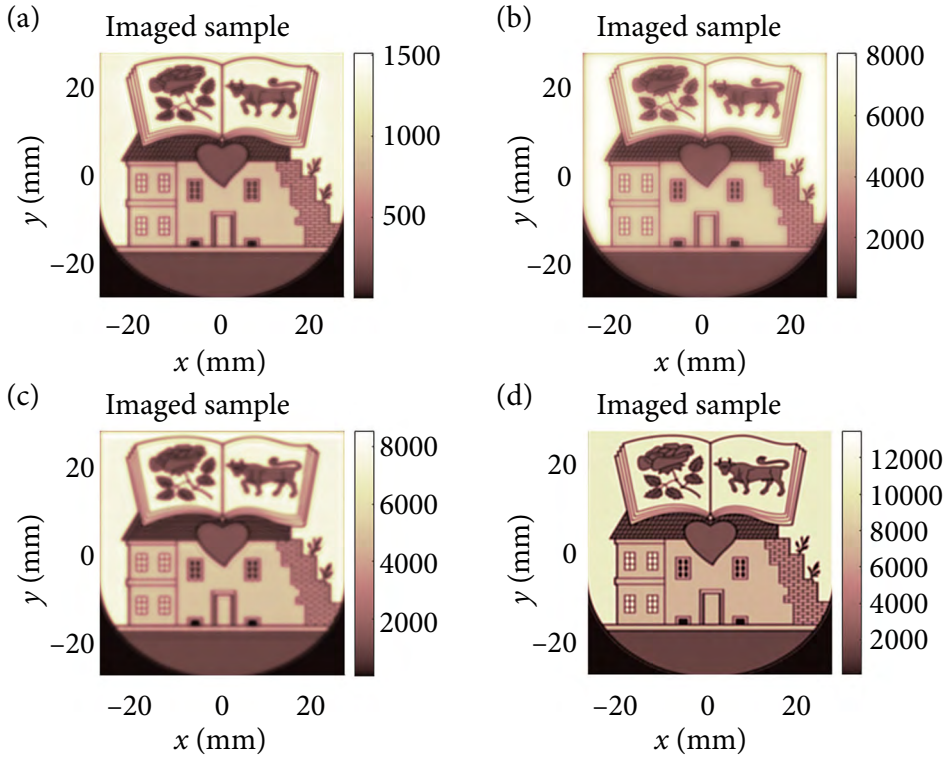


Fig. 5. Nonparaxial single-pixel THz imaging of the semi-transparent sample coat of arms of Ukmergė under different structured illuminations. Colour bars represent the recorded intensity of the sample image. The illumination is produced by the thin lens (a), the axicon (b), the Airy phase mask together with the lens (c) and the hyperbolical nonparaxial lens (d).

In this numerical experimentation, we suggest paying particular attention to the 'bright' and 'dark' windows in the object, the 'roof', 'brick wall', and to the 'rose' and the 'bull', as these are fine details with various levels of the modulation strengths. First, the thin lens is able to resolve the sample (see Fig. 5(a)). Some details look a bit blurred, and some details are not resolved. This is an expected behaviour, as there is a physical limitation on the spatial frequencies which can be resolved in such a system.

The axicon illumination can image the sample as well (see Fig. 5(b)). We note that the image now is brighter a few times, though the modulation levels from the original are somewhat flattened out. Most importantly, some fine details look now better resolved than in the previous case, pay attention to the subobjects in the picture.

The structured Airy illumination introduces further changes into the recorded image of the sample (see Fig. 5(c)). Most notably, the brick wall is now hard to resolve, but other objects of the same level of detail can be detected in the image. This is probably caused by the modulation transfer function of the imaging system being less sensitive to details of that spatial resolution. The image brightness is the same as in the previous case.

Moving our attention to the nonparaxial hyperbolic lens, we see that the sample is also successfully imaged (see Fig. 5(d)). Most importantly, we are able to increase the brightness almost 1.5 times compared to the previous two cases. Although, in general, a picture makes an impression of better quality, this is not so conclusive. Pay attention to the 'brick wall' – this detail seems to be badly resolved, while other fine details might look better than in previous cases.

In conclusion, we have successfully imaged intricate images that have a high contrast and a variable transparency with a single- pixel imaging technique that resolves the features of the image. For this purpose, we have introduced a nonparaxial hyperbolic lens, which we have used for Airy beam generation and both for the sample illumination and light direction to the detector. The results indicate that the modulation transfer function might depend not only on the spatial frequency of that modulation, but also on the strength of the modulation in the original object. This makes the assessment of the image quality of semitransparent objects not as straightforward as for objects with binary levels of modulation in transmission [13, 14]. Our findings indicate the need to perform more numerical and experimental studies on this topic, which are under review and will be presented elsewhere.

## Acknowledgements

This research has received funding from the Research Council of Lithuania (LMTLT), Agreement No. [S-MIP-23-71]. The authors acknowledge the support of colleagues from the Coherent Optics Laboratory throughout the discussions.

## References

[1] T.B. Pittman, Y. Shih, D. Strekalov, and A.V. Sergienko, Optical imaging by means of two-photon quantum entanglement, Phys. Rev. A **52**, R3429 (1995).

[2] J.H. Shapiro, Computational ghost imaging, Phys. Rev. A **78**, 061802 (2008).

[3] M.F. Duarte, M.A. Davenport, D. Takhar, J.N. Laska, T. Sun, K.F. Kelly, and R.G. Baraniuk, Single-pixel imaging via compressive sampling, IEEE Signal Process. Mag. **25**, 83 (2008).

[4] M.P. Edgar, G.M. Gibson, and M.J. Padgett, Principles and prospects for single-pixel imaging, Nat. Photonics **13**, 13 (2019).

[5] M.-J. Sun and J.-M. Zhang, Single-pixel imaging and its application in three-dimensional reconstruction: a brief review, Sensors **19**, 732 (2019).

[6] C.A. Osorio Quero, D. Durini, J. Rangel-Magdaleno, and J. Martinez-Carranza, Single-pixel imaging: An overview of different methods to be used for 3D space reconstruction in harsh environments, Rev. Sci. Instrum. **92**, 111501 (2021).

[7] R.F. Lyon, in: *Digital Photography II*, Vol. 6069 (SPIE, 2006) p. 606901.

[8] B.J. Logie, *Apparatus for Transmitting Views or Images to a Distance*, US Patent 1,699,270 (1929).

[9] P. Mertz and F. Gray, A theory of scanning and its relation to the characteristics of the transmitted signal in telephotography and television, Bell Syst. Tech. J. **13**, 464 (1934).

[10] H. Rubinsztein-Dunlop, A. Forbes, M.V. Berry, M.R. Dennis, D.L. Andrews, M. Mansuripur, C. Denz, C. Alpmann, P. Banzer, T. Bauer, et al.,

Roadmap on structured light, J. Opt. **19**, 013001 (2016).

[11] M. Mazilu, D.J. Stevenson, F. Gunn-Moore, and K. Dholakia, Light beats the spread: "non-diffracting" beams, Laser Photonics Rev. **4**, 529 (2010).

[12] Y. Shen, X. Wang, Z. Xie, C. Min, X. Fu, Q. Liu, M. Gong, and X. Yuan, Optical vortices 30 years on: OAM manipulation from topological charge to multiple singularities, Light Sci. Appl. **8**, 90 (2019).

[13] L. Minkevičius, D. Jokubauskis, I. Kašalynas, S. Orlov, A. Urbas, and G. Valušis, Bessel terahertz imaging with enhanced contrast realized by silicon multi-phase diffractive optics, Opt. Express **27**, 36358 (2019).

[14] R. Ivaškevičiūtė-Povilauskienė, P. Kizevičius, E. Nacius, D. Jokubauskis, K. Ikamas, A. Lisauskas, N. Alexeeva, I. Matulaitienė, V. Jukna, S. Orlov, et al., Terahertz structured light: nonparaxial Airy imaging using silicon diffractive optics, Light Sci. Appl. **11**, 326 (2022).

[15] K. Mundrys, S. Orlov, P. Kizevičius, L. Minkevičius, and G. Valušis, On evaluation of image quality in nonparaxial single-pixel imaging, Lith. J. Phys. **63**, 113 (2023).

[16] K. Iizuka, *Engineering Optics*, Springer Series in Optical Sciences, Vol. 35 (Springer, 2008).

[17] M. Born and E. Wolf, *Principles of Optics: Electromagnetic Theory of Propagation, Interference and Diffraction of Light* (Elsevier, 2013).

[18] W.J. Smith, *Modern Optical Engineering: The Design of Optical Systems* (McGraw-Hill Education, 2008).

## NEPARAKSIALINIS VIENO PIKSELIO PUSIAU PERMATOMŲ OBJEKTŲ VAIZDINIMAS NAUDOJANT PLOKŠČIĄ DIFRAKCINĘ OPTIKĄ

P. Kizevičius [a], S. Orlov [a], K. Mundrys [a], V. Jukna [a], L. Minkevičius [b], G. Valušis [b]

[a] *Fizinių ir technologijos mokslų centro Fundamentinių tyrimų skyrius, Vilnius, Lietuva*

[b] *Fizinių ir technologijos mokslų centro Optoelektronikos skyrius, Vilnius, Lietuva*

**Santrauka**

Didelės skaitinės apertūros lęšiai gali sukelti iškraipymus tradiciniame vaizdinime, todėl aukštos kokybės vaizdų gavimas gali būti sudėtingas ar net neįmanomas. Tačiau vieno taško vaizdinime ši problema minimizuojama pasitelkus įvairias vaizdo apšvietimo ir spinduliuotės surinkimo strategijas. Todėl įmanoma registruoti objektus su puikia skiriamąja geba, kontrastu ir ryškiu. Naujausi plokštieji fotoniniai elementai palengvino kompaktiškų neparaksialinių vaizdinimo sistemų kūrimą, kurie gali būti plačiai panaudoti optiniame diapazone. Ypač patrauklu juos naudoti THz bangų ilgių vaizdinime. Šios naujovės suteikia galimybę tobulėti tokiose srityse kaip komunikacija, medžiagų tikrinimas ir spektroskopija. Šiuo straipsniu pristatome pusiau skaidrių skirtingo detalumo objektų vieno taško vaizdinimą THz diapazone. Aprašome neparaksialinio plokščio hiperbolinio lęšio fazės skirstinį ir įvertiname jo veikimą įvairiuose vaizdinimo scenarijuose, lygindami jį su struktūrinio apšvietimo metodais, apimančiais Airy, Beselio ir plonojo lęšio konfigūracijas. Pateikiame išvadas apie galimus vaizdinimo patobulinimus siekiant geriausios vaizdinimo kokybės.